Journal of the Taiwan Institute of Chemical Engineers 45 (2014) 2469–2479

Contents lists available at ScienceDirect

Journal of the Taiwan Institute of Chemical Engineers

journal homepage: www.elsevier.com/locate/jtice

Photocatalytic degradation of ethyl violet dye mediated by TiO_2 under an anaerobic condition

Wen-Lian William Lee [b,c,*], Chung-Shin Lu [d], Ho-Pan Lin [a], Jau-Yan Chen [a], Chiing-Chang Chen [a,*]

[a] Department of Science Application and Dissemination, National Taichung University of Education, Taichung 403, Taiwan
[b] Department of Occupational Safety and Health, Chung-Shan Medical University, Taichung 402, Taiwan
[c] Department of Occupational Medicine, Chung Shan Medical University Hospital, Taichung 402,Taiwan
[d] Department of General Education, National Taichung University of Science and Technology, Taichung 40306, Taiwan

ARTICLE INFO

Article history:
Received 27 September 2013
Received in revised form 15 April 2014
Accepted 26 April 2014
Available online 2 June 2014

Keywords:
Photocatalytic reduction
TiO_2
BTEX
Ethyl violet

ABSTRACT

The TiO_2-mediated photocatalysis process has been successfully used for degrading dye pollutants during past decades. However, the dye degradation efficiency has been proposed to rely only on the concentration of oxygen molecules (through photooxidation pathway). In our current study, the dye ethyl violet (EV) degradation process is prepared under an anaerobic condition. Most interestingly, both photocatalytic reduction and photocatalytic oxidation intermediates are isolated and identified at the first time. Photoreduction intermediates such as benzene, toluene, ethylbenzene, and xylene (BTEX), ethane, and diethylamine are detected by Headspace-GC–MS. Moreover, 18 photodegraded intermediates are also identified and characterized through HPLC–PDA–ESI-MS. The results demonstrate that a novel photodegradation mechanism should be proposed *via* three competition pathways, including (i) the cleavage of the whole conjugated chromophore structure by photocatalytic reduction, (ii) the cleavage of the whole conjugated chromophore structure by photocatalytic oxidation, and (iii) *N*-de-ethylation of the chromophore skeleton.

© 2014 Taiwan Institute of Chemical Engineers. Published by Elsevier B.V. All rights reserved.

1. Introduction

Photocatalytic oxidation (PCO) of wastewater containing toxic organic compounds using TiO_2 has been extensively studied in recent years [1–11]. The TiO_2-mediated photocatalysis process has been successfully used for degrading dye pollutants during past decades [11,12]. However, the dye degradation efficiency has been proposed to rely only on the concentration of oxygen molecules (through photooxidation pathway). The ultimate objective of PCO is to convert the organic substrates to H_2O and CO_2. Photocatalytic reduction of CO_2 to formaldehyde, formic acid, methanol, and methane as the main products over semiconductor particles was demonstrated three decades ago [13,14]. H_2 production by semiconductor photocatalysts such as TiO_2 has attracted much attention. It represents a promising technology to use renewable resources for clean and environmentally friendly energy production [15–18]. Recently, with increasing concerns about climate change and the depletion of fossil fuels, there has been a revived interest in the production of H_2 by photocatalytic decomposition of organic substances [19–21]. These substances include biomass and its derivatives [22–25], such as cellulose, starch, sucrose, glucose, and glycerol, alcohols such as methanol, ethanol and C3-polyols [26,27]. The reaction condition is almost the same as that of PCO but without bubbling O_2 or air to suppress the thermal back-reaction of H_2 with O_2. H_2O, instead of O_2, is used as an oxidant for splitting organic compounds to H_2 and CO_2. The H_2 evolution rate is generally much higher than that of splitting pure water because of the presence of organic substances. As the process is analogous to the catalytic thermal reforming process, it is commonly called photocatalytic reforming (PR) reaction. Obviously, the reaction not only involves in the decomposition and mineralization of organic substrates, but also involves in the splitting of water to produce H_2. PR of C3-polyols and glucose for H_2 production over noble-metal-loaded TiO_2 was investigated by Wang et al. [27,28].

Hydrocarbon fuels are currently the most important source of energy due to their ready availability, stability, and high energy density [29]. An alternative to the traditional anaerobic digestion method of biogas production could generate methane and other

* Corresponding author. Tel.: +886 4 2218 3406; fax: +886 4 2218 3560.
E-mail addresses: wllee01@gmail.com (W.-L. Lee), ccchen@mail.ntcu.edu.tw, ccchen@ms3.ntcu.edu.tw (C.-C. Chen).

http://dx.doi.org/10.1016/j.jtice.2014.04.025
1876-1070/© 2014 Taiwan Institute of Chemical Engineers. Published by Elsevier B.V. All rights reserved.

useful hydrocarbons *via* photocatalytic reduction (PCR) [13,30–32]. Photocatalytic reduction of CO_2 to formaldehyde, formic acid, methanol, and methane as the main products over semiconductor particles was demonstrated three decades ago [13,33]. The photocatalytic generation of C_1–C_3 hydrocarbons and hydrogen from the aqueous solution of acetic acid over TiO_2 was investigated by Mozia et al. [34]. Acetic acid underwent the photo-Kolbe reaction yielding CH_4 and CO_2. Yuan et al. reported [35] that the findings were valuable not only in the molecular-level understanding of photocatalytic reactions over TiO_2-based photocatalysts, but also in the development of a green and benign photocatalytic route for the synthesis of esters directly from alcohols or from alcohols and aldehydes. Therefore, the gaseous mixture obtained during the photocatalytic reaction had a similar composition to that of biogas produced by a conventional anaerobic digestion method.

Dimitrijevic et al. [13] proposed that the water, both dissociated on the surface of TiO_2 and in subsequent molecular layers, had a threefold role of (i) stabilization of charges (preventing electron–hole recombination), (ii) an electron donor (reaction of water with photogenerated holes to give OH radicals), and (iii) an electron acceptor (formation of H atoms in a reaction of photogenerated electrons with protons on the surface, $-OH_2^+$).

Photocatalytic oxidation of EV for TiO_2 was investigated in our former work [36]. In this current study, the ethyl violet (EV) dye degradation process is prepared under an anaerobic condition to mimic the photo-Kolbe reaction. Most interestingly, both photocatalytic reduction and photocatalytic oxidation intermediates are isolated and identified at the first time under the anaerobic condition. Photoreduction intermediates such as benzene, toluene, ethylbenzene, and xylene (BTEX), ethane, and diethylamine are detected by Headspace-GC–MS. The photocatalytic reduction and reforming seem playing an important role in the generation of BTEX. Moreover, 18 photooxidation intermediates are also identified and characterized through HPLC–PDA–ESI-MS. According to the results, a possible mechanism for the process is suggested and discussed.

2. Experiment

2.1. Materials and reagents

The P25 TiO_2 nanoparticles were supplied by Degussa. Standards of the following compounds were used as standard compounds, including benzene (99%), toluene (99%), *o*-xylene (99%), *m*-xylene (99%), *p*-xylene (99%), and ethylbenzene (99%) from Acros. 4-Aminophenol (AP; analytical standard) was purchased from Riedel-de Haen. The 4-(*N*,*N*-diethylamino)-4′-(*N*′,*N*′-diethylamino)benzophenone (DDBP) was obtained from Tokyo Kasei Kogyo Co. The stock solutions of these compounds were prepared separately at a concentration of 2 mg/mL in methanol. These stock standard solutions were diluted with methanol weekly to prepare a mixed stock solution with a concentration of 0.1 mg/mL for each compound. The standard solution containing the required amount of each analyte (0.5–200 ng/mL) was prepared daily by diluting the mixed standard solution with double distilled water to study the extraction performance under different conditions. Stock and working standards were stored at 4 °C. 1,4-Difluorobenzene (Merck), and EV dye (TCI) were obtained and used without any further purification.

2.2. Instruments and analytic methods

FE-SEM–EDS measurements were carried out with a field-emission microscope (JEOL JSM-7401F) at an acceleration voltage of 15 kV. The BET specific surface areas of the samples were measured with an automatic system (Micromeritics Gemini 237 °C) using nitrogen gas as the adsorbate, at liquid nitrogen temperature. Electron paramagnetic resonance signals were recorded with a Bruker EMX-10/12.

The Headspace-GC–MS system was equipped with an AutoSystem XL Gas Chromatograph, a PerkinElmer TurboMass Gold Mass Spectrometer, and Turbomatrix 40 Headspace Samplers. Under nitrogen condition, 20-mL Headspace-GC vials were filled with 10-mL aliquots of 10 ppm EV with 1 mg of TiO_2 powder and sealed with gas-tight polytetrafluoroethylene (PTFE)-lined rubber septum caps after acidification or alkalization. Each sample was heated for the same period of time at the same temperature in the pre-heating module. The tested prewarm temperatures were 70 and 80 °C with prewarm time 2, 5, 7, 10 and 30 min for the highest sensitivity and reproducibility of the headspace analysis. The photodegradated intermediates in the vapor were partitioned between the liquid and the gaseous phase. The gaseous phase was transferred into the column. The separation was carried out in a DB-5 capillary column (5% diphenyl/95% dimethyl-siloxane), 60 m, 0.25-mm i.d., and 1.0-μm thick film. A split–splitless injector was used under the conditions of injection volume 10 μL, injector temperature 280 °C, and split flow 10 mL/min. The helium carrier gas flow was 1 mL/min. The oven temperature program was 4.0 min at 40 °C, 4 °C/min to 80 °C (2 min), and 8 °C/min to 280 °C (9 min). Typical MSD operating conditions were optimized by the autotuning software. Electron impact (EI) mass spectra were monitored from 35 to 300 m/z. The ion source and inlet line temperatures were set at 220 °C and 280 °C, respectively.

Waters ZQ LC/MS system was used for identifying the reaction intermediates. After each irradiation cycle, the amount of residual dye was thus determined by HPLC. The analyses of organic intermediates were accomplished by HPLC–ESI-MS after readjusting chromatographic conditions in order to make the mobile phase compatible with the working conditions of the mass spectrometer. Solvent A was 25 mM aqueous ammonium acetate buffer (pH 6.9), and solvent B was methanol. LC was carried out on an Atlantis™ dC18 column (250 mm × 4.6 mm i.d., dp = 5 μm). The mobile phase flow rate was 1.0 mL/min. A linear gradient was run as $t = 0$, $A = 95$, $B = 5$; $t = 20$, $A = 50$, $B = 50$; $t = 35$–40, $A = 10$, $B = 90$; $t = 45$, $A = 95$, $B = 5$. The column effluent was introduced into the ESI source of the mass spectrometer. The quadruple mass spectrometer, equipped with an ESI interface with heated nebulizer probe at 350 °C, was used with an ion source temperature of 80 °C. ESI was carried out with the vaporizer at 350 °C, and nitrogen was used as sheath (80 psi) and auxiliary (20 psi) gas to assist in the preliminary nebulization and to initiate the ionization process. A discharge current of 5 A was applied. Tube lens and capillary voltages were optimized for the maximum response during the perfusion of the EV standard.

The formation of hydroxyl radicals ($^{\bullet}OH$) in the TiO_2 system was detected by the fluorescence technique using coumarin as a probe molecule. The experimental procedures were similar to those used in the measurement of photocatalytic activities except that the aqueous solution of EV was replaced by an aqueous solution of 1×10^{-3} M coumarin. The UV light irradiation was continuous and the sampling was performed every 2 h for analyses. The solution was analyzed after the filtration on a Shimadzu RF-5301PC fluorescence spectrophotometer. The product of the coumarin hydroxylation, 7-hydroxycoumarin (7HC), gave a peak at a wavelength of about 456 nm by excitation with a wavelength of 332 nm.

2.3. Photocatalytic reaction

Under nitrogen condition, 20-mL Headspace-GC vials were filled with 10-mL aliquots of 10 ppm EV with 1 mg TiO_2 powder and sealed with gas-tight polytetrafluoroethylene (PTFE)-lined rubber septum caps after acidification or alkalization. Irradiations were carried out using two UV-365 nm lamps (20 W). An average irradiation intensity of 5.8 W/m^2 was maintained throughout the experiments and was measured by the internal radiometer. The results obtained were more likely different from that of PCO of EV over TiO_2 under a N_2 condition, *i.e.*, O_2 free condition. Therefore, it was essential to conduct a separate GC–MS and HPLC–MS measurement to study the photodegraded mechanism.

3. Results and discussion

3.1. Characterization of P25-TiO_2

Titanium dioxide (P25) – a known mixture of 80% anatase and 20% rutile, with an average particle size of 30 nm, nonporous, and with a reactive surface area of 50 ± 10 m^2/g – was used as received for all degradation experiments and supplied by Degussa Co. The surface morphologies of the P25-TiO_2 powder were examined with FE-SEM-EDS, and the results demonstrated a highly uniform dispersion in Fig. S1 of Supplementary materials. The EDS results showed that the main elements of these samples were titanium and oxygen. In addition, the BET specific surface area and pore volume of the TiO_2-powder material showed 55.42 m^2/g and 0.018 cm^2/g for Degussa P25. UV–vis diffuse reflectance spectra of different catalysts are shown in Fig. S2 of Supplementary materials. The observed results of the P25-TiO_2 diffuse reflection spectra showed obvious absorption in the visible light region up to about 425 nm. E_g of P25-TiO_2 was determined from a plot of $(\alpha h\upsilon)$ *vs* energy $(h\upsilon)$ in Fig. S2 (inset) of Supplementary materials and elicited to be 3.07 eV, indicating that the P25-TiO_2 had a band gap suitable for the photocatalytic degradation of organic contaminants under UV-light irradiation [37,38].

Supplementary figure related to this article can be found, in the online version, at http://dx.doi.org/10.1016/j.jtice.2014.04.025.

Supplementary figure related to this article can be found, in the online version, at http://dx.doi.org/10.1016/j.jtice.2014.04.025.

3.2. UV–visible spectra

The aqueous solution of the EV dye was a little unstable under UV irradiation in the absence of TiO_2. However, the EV dye could be degraded efficiently in aqueous EV/TiO_2 dispersions by UV light irradiation at 365 nm under an anaerobic condition. After the irradiation for 20 h, *ca.* 99.9% of the EV dye was degraded in Fig. 1. During UV irradiation, the characteristic absorption band of the dye around 593.0 nm decreased rapidly with a slight hypsochromic shift (579.8 nm), but no new absorption band appeared even in the ultraviolet range ($200\ \text{nm} < \lambda < 400\ \text{nm}$), indicating the possible formation of a series of *N*-de-ethylated intermediates, cleavage of the whole conjugated chromophore structure of the EV dye, and degradation of the phenylic skeleton. Similar phenomena were also observed during the TiO_2-mediated photodegradation of ethyl violet [12] and crystal violet [39] under visible irradiation.

3.3. GC–MS analysis

It is still impossible to real-time investigate the PR process of these systems *in situ*. A relatively feasible way at present was to use GC–MS and HPLC–MS for identifying both the PCO and PCR intermediates (both liquid- and gas-phase intermediates) although the reaction conditions were not exactly the real reforming

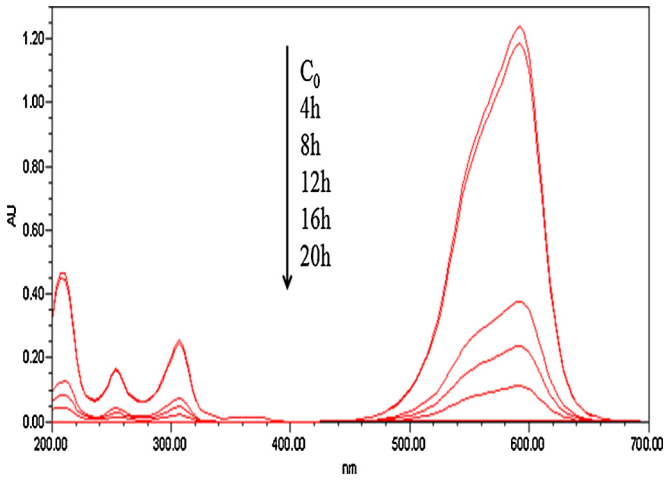

Fig. 1. UV–vis spectra change of EV in aqueous TiO_2 dispersions (EV: 10 mg/L, TiO_2: 10 mg/L) as a function of irradiation time. Spectra from top to bottom correspond to the irradiation time of 4 h, 8 h, 12 h, 16 h, and 20 h, respectively.

reaction. The intermediates were marked in the GC chromatograms (Fig. 2) and the relevant mass spectra are illustrated in Table 1. Up to six compounds could be detected as possible degradation intermediates in Fig. 2.

The intermediates were marked in the GC–MS/EI chromatogram (Fig. 2). Table 1 presents the fragmentation patterns of the intermediates (I–VI) and the corresponding compounds identified by the interpretation of their MS spectra. The peaks eluting at 31.91, 30.39, 29.96, 24.57, and 18.35 min during GC–MS were identified as *o*-xylene, *m*-, *p*-xylene, ethylbenzene, toluene, and benzene with fit values of 91%, 87%, 89%, 90%, and 95%, respectively, found by searching the mass spectra library. Further oxidation of organic substrates containing nitrogen to nitrate could be obtained by increasing irradiation time.

3.4. HPLC–PDA–ESI-MS analysis

Temporal variations occurring in the solution of EV dye during the degradation process with UV irradiation were examined using HPLC coupled with a photodiode array detector and ESI mass spectrometry. The chromatograms at pH 6 are illustrated in Fig. 3, recorded at 580, 350, and 300 nm. Eighteen components were

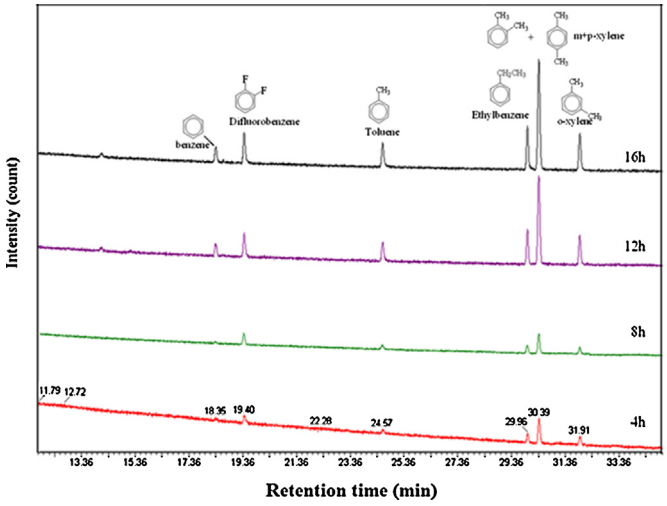

Fig. 2. Variation in the relative distribution of the products obtained at gas phase from the photocatalytic reduction of EV as a function of irradiation time.

Table 1
Identification of the intermediates from the photodegradation of EV by HPLC–ESI-MS or GC–EI-MS.

HPLC peaks	Intermediates	Abbreviation	MS peaks (*m*/*z*)	Absorption maximum (nm)
A	*N*,*N*,*N*′,*N*′,*N*″,*N*″-Hexaethylpararosaniline	EV	456.51	592.2
B	*N*,*N*-Diethyl-*N*′,*N*′-diethyl-*N*″-ethylpararosaniline	DDEPR	428.48	584.9
C	*N*,*N*-Diethyl-*N*′-ethyl-*N*″-ethylpararosaniline	DEEPR	400.46	583.6
D	*N*,*N*-Diethyl-*N*′,*N*′-diethylpararosaniline	DDPR	400.52	584.4
E	*N*-Ethyl-*N*′-ethyl-*N*″-ethyl pararosaniline	EEEPR	372.44	580.5
F	*N*,*N*-Diethyl-*N*′-ethylpararosaniline	DEPR	372.37	581.5
G	*N*-Ethy-*N*′-ethylpararosaniline	EEPR	344.41	570.2
H	*N*,*N*-Diethylpararosaniline	DPR	344.41	570.5
I	*N*-Ethylpararosaniline	EPR	316.39	544.5
a	4-(*N*,*N*-Diethylamino)-4′-(*N*′,*N*′-diethylamino) benzophenone	DDBP	325.41	379.5
b	4-(*N*,*N*-Diethylamino)-4′-(*N*′-ethylamino)benzophenone	DEBP	297.38	373.1
c	4-(*N*-Ethylamino)-4′-(*N*′-ethylamino)benzophenone	EEBP	269.29	365.5
d	4-(*N*,*N*-Diethylamino)-4′-aminobenzophenone	DBP	269.29	372.1
e	4-(*N*-Ethylamino)-4′-aminobenzophenone	EBP	241.33	357.2
f	4,4′-Bis-aminobenzophenone	BP	213.17	344.2
α	4-(*N*,*N*-Diethylamino)phenol	DAP	166.21	305.7
β	4-(*N*-Ethylamino)phenol	EAP	N/A	289.2
γ	4-Aminophenol	AP	N/A	281.9
	Benzene	BZ	78.11	N/A
	Toluene	TOL	92.14	N/A
	Ethyl benzene	EB	106.16	N/A
	Xylene	DMB	106.17	N/A

identified, with the retention time less than 55 min. The EV dye and its related intermediates are denoted as species A–I, a–f, and α–γ. Except for the initial EV dye (peak A), the other peaks initially increase before subsequent decrease, indicating the formation and transformation of the intermediates. The *N*-de-ethylation of the EV dye has the wavelength position of its major absorption band move toward the blue region. The oxidative degradation yields 4-diethylaminophenol (DAP), 4-diethylamino-4′-diethyl-aminobenzophenone (DDBP), and their *N*-de-ethylated products. The *N*-de-ethylation of the DDBP, produced by cleaving the EV chromophore ring structure, has the wavelength position of its major absorption band move toward the blue region.

The absorption spectra of each intermediate in the visible and ultraviolet spectral region are depicted in Table 1. They were identified as A–I corresponding to the peaks A–I in Fig. 3(a). The other intermediates were identified as a–f and α–γ, corresponding to the peaks a–f and α–γ in Fig. 3(b) and (c), respectively. The absorption maximum of the spectral bands shifted from 592.1 nm (spectrum A) to 544.5 nm (spectrum I), from 379.5 nm (spectrum a) to 344.2 nm (spectrum f), and from 305.7 nm (peak α) to 281.9 nm (peak γ). These shifts of the absorption band were presumed to result from the formation of series of *N*-de-ethylated intermediates. From these results, several groups of intermediates could be distinguished.

The first group was marked in the chromatogram and illustrated in Fig. 3(a). The *N*-de-ethylation of the *N*,*N*,*N*′,*N*′,*N*″,*N*″-hexaethyl-pararosaniline (EV) dye had the wavelength position of its major absorption band moving toward the blue region, λ_{max}, **A** (EV), 592.2 nm; **B**, *N*,*N*-diethyl-*N*′,*N*′-diethyl-*N*″-ethylpararosaniline, 584.9 nm; **C**, *N*,*N*-diethyl-*N*′,*N*′-diethylpararosaniline, 583.6 nm; **D**, *N*,*N*-diethyl- *N*′-ethyl-*N*″-ethylpararosaniline, 584.4 nm; **E**, *N*,*N*-diethyl-*N*′-ethyl-pararosaniline, 580.5 nm; **F**, *N*-ethyl-*N*′-ethyl-*N*″-ethylpararosaniline, 581.5 nm; **G**, *N*,*N*-diethylpararosaniline, 570.2 nm; **H**, *N*-ethyl-*N*′-ethylpararosaniline, 570.5 nm; **I**, *N*–ethyl-pararosaniline, 544.5 nm. The *N*-de-ethylation of the EV dye caused the wavelength shifts depicted in Table 1 because of the attack by one of the active oxygen species on the *N*,*N*-diethyl or *N*-ethyl group. The examination of Supporting information suggested that the EV dye was *N*-de-ethylated in a stepwise manner by *N*-hydroxyethylated intermediate (*i.e.*, ethyl groups were removed one by one as confirmed by the gradual peak wavelength shifting toward the blue region), which was reported [40].

The second group was marked in the chromatogram and illustrated in Fig. 3(b). Destruction of EV yielded DAP, DDBP, and their *N*-de-ethylated products. The *N*-de-ethylation of the DDBP species, produced by the cleavage of the EV chromophore ring structure, had the wavelength position of its major absorption band move toward the blue region, λ_{max}, **a**, 4-(*N*,*N*-diethylamino)-4′-(*N*′,*N*′-diethylamino)benzophenone, 379.5 nm; **b**, 4-(*N*,*N*-diethylamino)-4′-(*N*′-ethylamino)benzophenone, 373.1 nm; **c**, 4-(*N*-ethylamino)-4′-(*N*′-ethylamino)benzophenone, 365.5 nm; **d**, 4-(*N*,*N*-diethylamino)-4′-aminobenzophenone, 372.1 nm; **e**, 4-(*N*-ethylamino)-4′-aminobenzophenone, 357.2 nm; **f**, 4,4′-bis-aminobenzophenone, 344.2 nm. The proposed intermediate (**a**) was compared with the standard material of 4-(*N*,*N*-diethylamino)-4′-(*N*′,*N*′-diethylamino)benzophenone. The retention time and absorption spectra were identical.

The third group was marked in the chromatogram and illustrated in Fig. 3(c). The *N*-de-ethylation of the DAP, produced by the cleavage of the EV chromophore ring structure, had the wavelength position of its major absorption band move toward the blue region, λ_{max}, **α**, 4-(*N*,*N*-diethylamino)phenol, 305.7 nm; **β**, 4-(*N*-ethylamino)phenol, 289.2 nm; **γ**, 4-aminophenol, 281.9 nm. The proposed intermediate (**γ**) was compared with the standard material of 4-aminobenzophenone. The retention time and absorption spectra were identical.

The photodegraded intermediates were further identified using the HPLC–ESI mass spectrometric method. The molecular ion peaks appeared in the acid forms of the intermediates. Results of HPLC–ESI mass spectra are summarized in Table 1. The molecular ion peaks appeared the acid forms of the intermediates. The results of mass spectral analyses confirmed that the component **A**, *m*/*z* = 456.51, in liquid chromatogram was the EV dye. The other components were **B**, *m*/*z* = 428.48; **C**, *m*/*z* = 400.46; **D**, *m*/*z* = 400.52; **E**, *m*/*z* = 372.44; **F**, *m*/*z* = 372.37; **G**, *m*/*z* = 344.41; **H**, *m*/*z* = 344.41; **I**, *m*/*z* = 316.39; **a**, *m*/*z* = 325.41; **b**, *m*/*z* = 297.38; **c**, *m*/*z* = 269.29; **d**, *m*/*z* = 269.29; **e**, *m*/*z* = 241.33; **f**, *m*/*z* = 213.17; **α**, *m*/*z* = 166.21. The results of HPLC chromatograms, UV–visible spectra, HPLC–ESI and GC–EI mass spectra are summarized in Table 1.

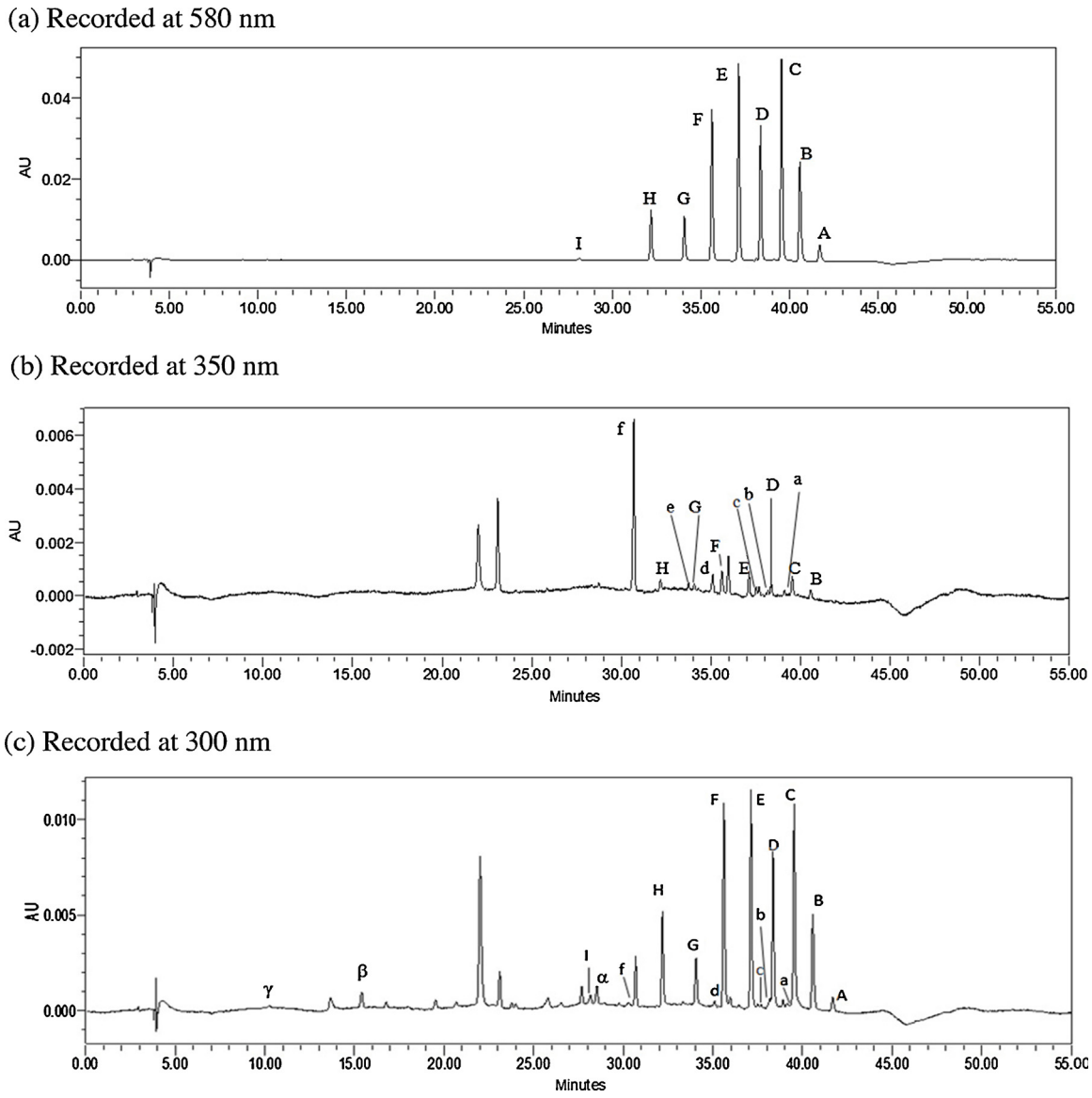

Fig. 3. HPLC chromatogram of the intermediates at liquid phase with TiO_2 1 mg, at pH 6, at 8 h of irradiation, recorded at (a) 580, (b) 350, and (c) 300 nm.

These species corresponded to the intermediates that possessed from two to four fewer ethyl groups relative to the EV dye and were correlative with three pairs of isomeric molecules. One of these isomers, DMMPR, was formed by the removal of an ethyl group from two different sides of the EV molecule, while the other isomer in this pair, DDPR, was produced by the removal of two ethyl groups from the same side of the EV structure. In the second pair of isomers, EEEPR was formed by the removal of an ethyl group from each side of the EV molecule, and the other, DEPR, was produced by the removal of both two ethyl groups from the same side of the EV structure and an ethyl group from the other side of the EV structure. The third pair of isomers, DPR, was formed by the removal of two ethyl groups from two different sides of the EV molecule, while EEPR was produced by the removal of two ethyl groups from the same side of the EV structure and of an ethyl group from the rest of two sides of the EV structure. Both intermediates displayed identical HPLC–ESI-MS characteristics. Considering that the polarity of DDPR, DEPR, and DPR species exceeded that of the DEEPR, EEEPR and EEPR intermediates, the latter were expected to be eluted after the DDPR, DEPR and DPR species. Additionally, to the extent that two *N*-ethyl groups were stronger auxochromic moieties than either *N*,*N*-diethyl or amino groups, the maximal absorption of the DDPR, DEPR and DPR intermediates was anticipated to occur at the wavelengths shorter than the band position of DEEPR, EEEPR and EEPR species. The following results and the proposed mechanism support this argument.

3.5. EV dye photodegradation mechanisms

The relative distribution of all intermediates obtained is illustrated in Fig. 4. To minimize errors, the relative intensities were recorded at the maximum absorption wavelength for each intermediate although the complete quantitative determination of all photogenerated intermediates was not achieved, owing to unavailable appropriate molar extinction coefficients of these intermediates and unavailable reference standards. Nonetheless, it was clearly observed the changes in the distribution of each intermediate during the photodegradation of EV.

To understand the active species involving in the photocatalytic process, hydroxyl radicals ($^{\bullet}OH$) were detected in the TiO_2/UV

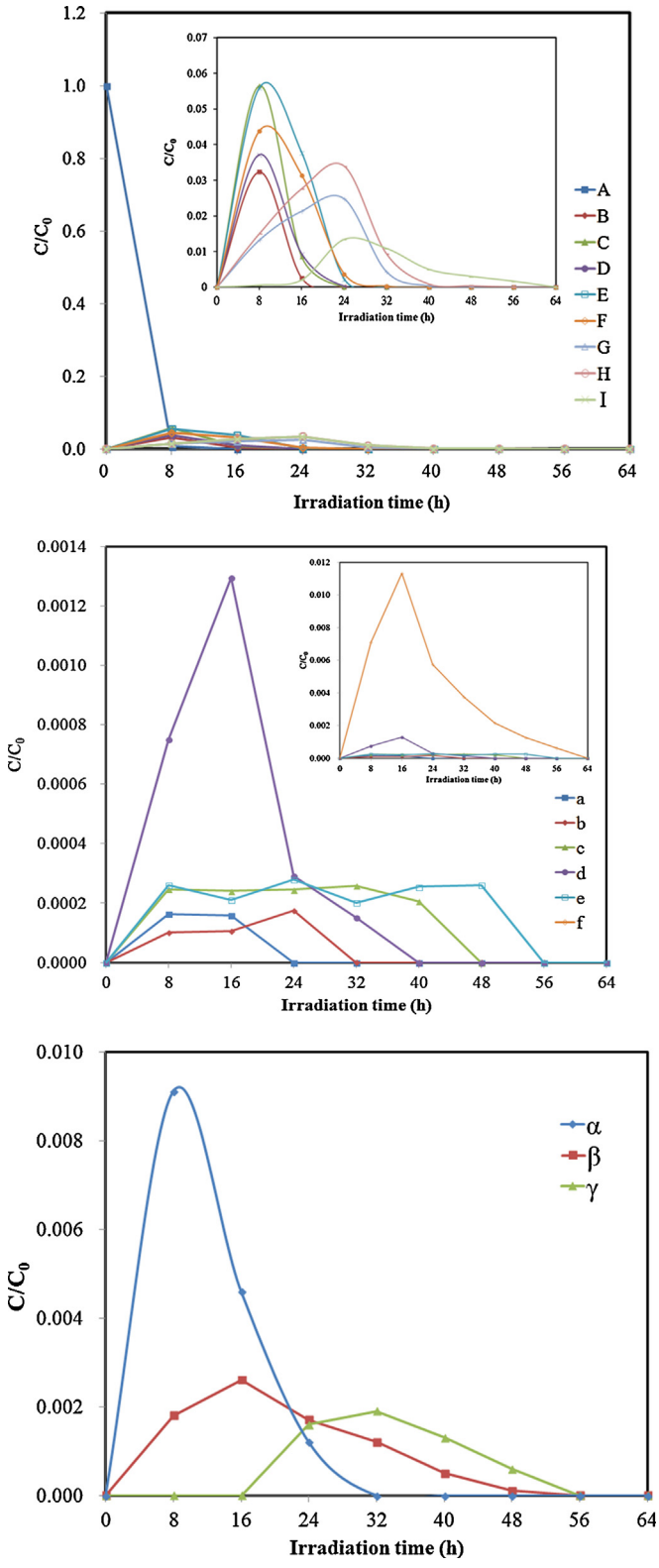

Fig. 4. Variation in the relative distribution of the photodegraded products obtained from the photodegradation of EV as a function of irradiation time. Curves A–I, a–f, and α–γ correspond to the peaks A–I, a–f, and α–γ in Fig. 3, respectively.

system under an anaerobic (or aerobic) condition by the PL technique using coumarin as a probe molecule. Coumarin readily reacted with •OH to produce a highly fluorescent product, 7HC [41,42]. Fig. 5 shows the changes of the fluorescence spectra from 10^{-3} M coumarin solution under UV-light irradiation with the

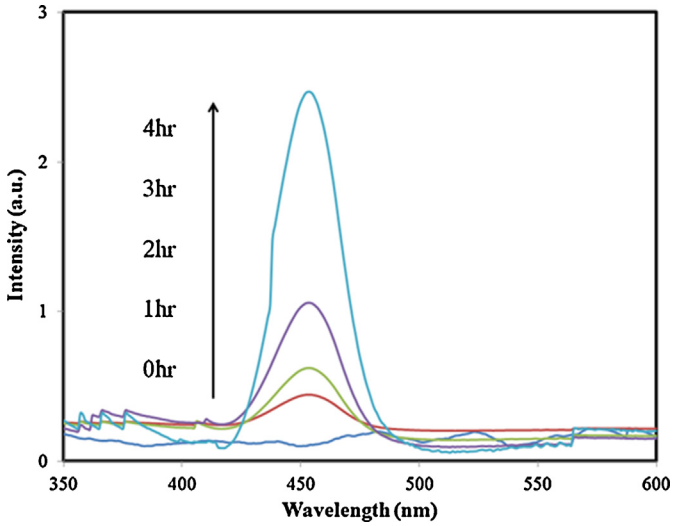

Fig. 5. Fluorescence spectral changes observed during the illumination of TiO_2 in a 1×10^{-3} M aqueous solution of coumarin (excitation at 332 nm). Each fluorescence spectrum is recorded every 1 h of UV-light irradiation.

irradiation time in the presence of TiO_2 under an anaerobic (or aerobic) condition. A gradual increase in the fluorescence intensity at about 456 nm was observed with increasing irradiation time. The generated fluorescence spectrum had the identical shape and maximum wavelength with those of the standard 7HC. This suggested that the fluorescent product 7HC was formed during TiO_2 photo-catalysis due to the specific reaction between •OH and coumarin. Therefore, •OH was shown to be the active species during TiO_2 photocatalytic reaction under an anaerobic (or aerobic) condition.

Dimitrijevic et al. [13] proposed that the water, both dissociated on the surface of TiO_2 and in subsequent molecular layers, had a threefold role of (i) stabilization of charges (preventing electron–hole recombination), (ii) an electron donor (reaction of water with photogenerated holes to give •OH radicals), and (iii) an electron

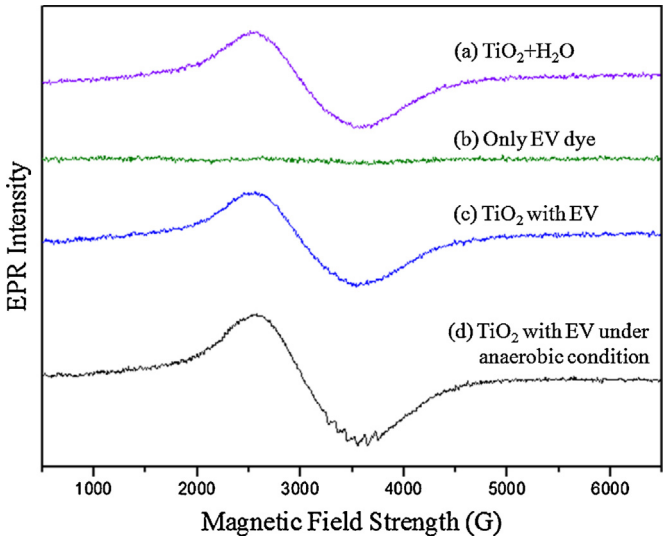

Fig. 6. EPR spectra recorded at room temperature after 1 min of illumination of TiO_2 in (a) H_2O, (c) with EV under an anaerobic condition, (d) with EV under an aerobic condition, and (b) 10 mg aqueous EV only. Power, 33.2 mW; modulation amplitude, 0.1 mT; light source, 300-W Xe lamp. A capillary tube is filled with a solution of TiO_2 (20 mg/mL) and DMPO (60 mM) and placed in a vacuum, 4 mm diameter Suprasil tube.

acceptor (formation of H atoms in a reaction of photogenerated electrons with protons on the surface, $-OH_2^+$).

EPR spectroscopy has been widely used for examining paramagnetic species formed upon band-gap excitation of TiO_2, including P25-TiO_2 [13,43,44]. In Fig. 6(a), EPR spectra were recorded following the irradiation of TiO_2 suspensions with pulsed laser illumination at 355 nm. A spectrum displaying signal was obtained, showing that the $^{\bullet}OH$ radical was indeed formed under anaerobic conditions. As illustrated in spectrum (b) of Fig. 6, no signal was obvious in EV aqueous under anaerobic conditions, whereas $^{\bullet}OH$ radical signals were quite obvious in irradiated aqueous TiO_2 dispersions with EV under anaerobic (or aerobic) conditions (spectrum (c) and (d) of Fig. 6). These observations demonstrated that the $^{\bullet}OH$ radical formed during the photodegradation process under anaerobic (or aerobic) conditions. However, Dimitrijevic et al. [13] proposed that the water, both dissociated on the surface of TiO_2 and in subsequent molecular layers, had a threefold role of (i) stabilization of charges (preventing electron–hole recombination), (ii) an electron donor (reaction of water with photogenerated holes to give $^{\bullet}OH$ radicals), and (iii) an electron acceptor (formation of $^{\bullet}H$ atoms in a reaction of photogenerated electrons with protons on the surface, $-OH_2^+$). For the above reasons, $^{\bullet}OH$ radicals and $^{\bullet}H$ atoms were subsequently produced under the anaerobic condition, as shown in Eqs. (1)–(5).

$$TiO_2 + h\nu \rightarrow h^+ + e^- \quad (1)$$

$$h^+ + H_2O \rightarrow {}^{\bullet}OH + H^+ \quad (2)$$

$$h^+ + OH^- \rightarrow {}^{\bullet}OH \quad (3)$$

$$e^- + H_2O \rightarrow {}^{\bullet}H + {}^{\bullet}OH \quad (4)$$

$$e^- + H^+ \rightarrow {}^{\bullet}H \quad (5)$$

These cycles continuously occurred when the system was exposed to UV-light irradiation; after several cycles of photo-oxidation and -reduction, the degradation of EV dye by the formed oxidant and reductant species could be expressed by Eqs. (6)–(10):

$$EV + {}^{\bullet}H \rightarrow \text{reductiveproducts} \quad (6)$$

$$EV + {}^{\bullet}OH \rightarrow \text{oxidativeproducts} \quad (7)$$

$$EV + h+ \rightarrow EV^{+\bullet} \rightarrow \text{degradedcompounds} \quad (8)$$

$$EV^{+\bullet} + {}^{\bullet}OH \rightarrow \text{degradedcompounds} \quad (9)$$

$$EV^{+\bullet} + {}^{\bullet}H \rightarrow \text{degradedcompounds} \quad (10)$$

Serpone et al. [45] suggested that *N*-de-ethylation was caused by an attack of active oxygen species on *N*-ethyl groups under aerobic conditions. Like UV irradiation with aerobic conditions, most $^{\bullet}OH$ was generated directly from the reaction between the holes and surface-adsorbed H_2O or OH^-, the only pathway for the formation of reductive species under UV-light irradiation was through the reduction of H_2O or H^+ by the conduction band electron. De-ethylation of the EV dye occurred mostly through the attack by $^{\bullet}OH$ species, which were a perfect nucleophilic reagent, on the *N*-ethyl portion of EV. Additionally, considering that the *N*,*N*-diethyl group in DDPR, DEPR and DPR was bulkier than the *N*-ethyl group in DEEPR, EEEPR and EEPR molecules, the nucleophilic attack by $^{\bullet}OH$ on the *N*-ethyl group should be favored at the expense of the *N*,*N*-diethyl group. In accord with this notion, the HPLC results showed that the DDPR, DEPR, and DPR intermediates reached the maximal concentration before the DEEPR, EEEPR, and EEPR intermediates did. However, considering that the attack probability of the two *N*,*N*-diethyl groups in DDEPR being higher than the one *N*-ethyl group in DDEPR molecules, the nucleophilic attack by $^{\bullet}OH$ on the *N*,*N*-diethyl group should be favored at the *N*-ethyl group. The *N*-di-de-ethylated intermediates (DEEPR and DDPR) were clearly observed (Fig. 4, curves C and D) that DEEPR and DDPR reached their maximum concentration at the same time after an 8-h irradiation period because of the two competitive factors mentioned above. The *N*-tri-de-ethylated intermediates (EEEPR and DEPR) were clearly observed (Fig. 4, curves E and F) that EEEPR reached its maximum concentration after an 8-h irradiation period, while DEPR reached its maximum concentrations after 8-h because $^{\bullet}OH$ attacked the *N*-ethyl group of DEEPR and the *N*,*N*-diethyl group of DDPR. The *N*-tetra-de-ethylated intermediates (EEPR and DPR) were clearly observed (Fig. 4, curves G and H) that EEPR reached its maximum concentration after a 24-h irradiation period because $^{\bullet}OH$ attacked the *N*-ethyl group of EEEPR and the *N*,*N*-diethyl group of DEPR, while DPR reached its maximum concentrations after a 24-h irradiation period because $^{\bullet}OH$ attacked the *N*-ethyl group of DEPR. In the *N*-penta-de-ethylated intermediates (EPR), curve I in Fig. 4, EPR reached its maximum concentration after an 28-h irradiation period because $^{\bullet}OH$ attacked the *N*-ethyl group of EEPR and the *N*,*N*-diethyl group of DPR. The successive appearance of the maximal quantity of each intermediate indicated that the *N*-de-ethylation of EV was a stepwise photochemical process that occurred by a de-hydroxylation of *N*-hydroxyethylated intermediates.

The oxidative degradation of EV dye occurred mostly through the attack by $^{\bullet}OH$ species on the central carbon portion of EV and produced DDBP and DAP under acidic aqueous conditions. The evolution of the concentration of the initial dye and identified intermediates was followed as a function of irradiation time. The result is displayed in Fig. 4. The oxidative degradation intermediates DDBP and DAP were clearly observed (Fig. 4, curves a and α) to reach their maximum concentrations at the same time after an 8-h irradiation period. The *N*-mono-de-ethylated intermediates DEBP and EAP were clearly observed (Fig. 4, curves b and β) to reach their maximum concentrations at the same time after a 16-h irradiation period. The *N*-di-de-ethylated intermediates EEBP and AP were clearly observed (Fig. 4, curves c, d and γ) to reach their maximum concentrations after a 24-h irradiation period while DBP reached its after 4 h because $^{\bullet}OH$ attacked the *N*-ethyl group of DEBP and the *N*,*N*-diethyl group of DEBP. The other *N*-ethylated intermediates, EBP and BP, were clearly observed (Fig. 4, curves e and f) to reach their maximum concentrations after 40-h and 48-h irradiation periods, respectively. The concentrations of the other hydroxylations of *N*-ethylated intermediates might be under the detectable limit.

According to earlier reports [45,46], most oxidative *N*-de-alkylation processes were preceded by the formation of a nitrogen-centered radical while the destruction of dye chromophore structures was preceded by the generation of a carbon-centered radical [46–49]. When the degradation of EV was consistent, it would occur *via* two different photooxidation pathways (destruction of the chromophore structure and *N*-de-ethylation) due to the formation of different radicals (either a carbon-centered or nitrogen-centered radical). It was no doubt that the electron injection from the dye to the conduction band of TiO_2 yielded the dye cation radical, a process determined by the nature of the HOMO orbital of the excited dye, dye* [50]. After this step, the cation radical, $Dye^{\bullet+}$, could undergo hydrolysis and/or deprotonation pathways of the dye cation radicals, which in turn were determined by different adsorption modes of EV on the TiO_2 particle surface.

On the basis of all experimental results above, the dye molecule in the EV/TiO_2 system was adsorbed through the positively charged diethylamine function. Following the electron injection

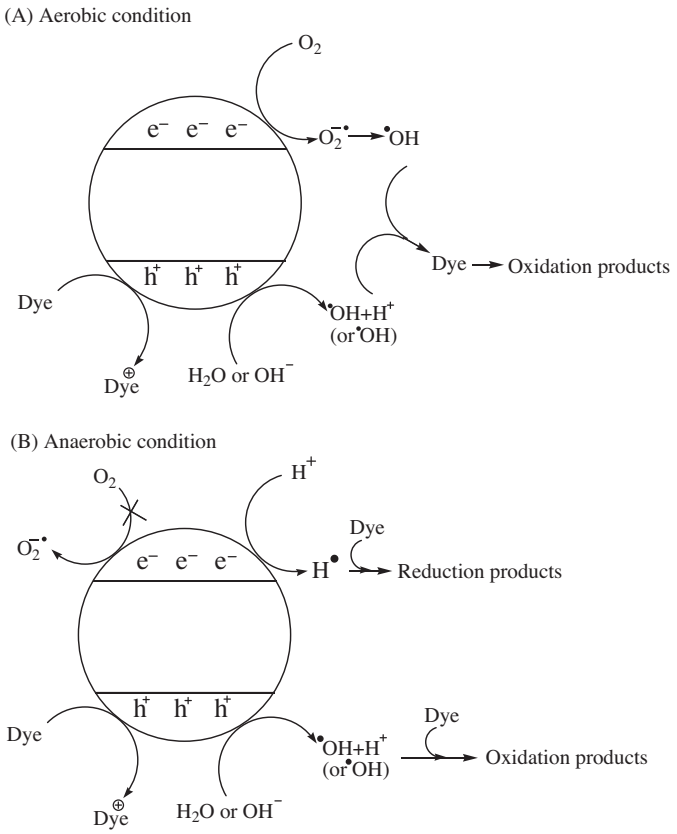

Fig. 7. Schematic representations of the possible mechanisms of photocatalytic degradation of EV with TiO_2 under (A) aerobic and (B) anaerobic conditions.

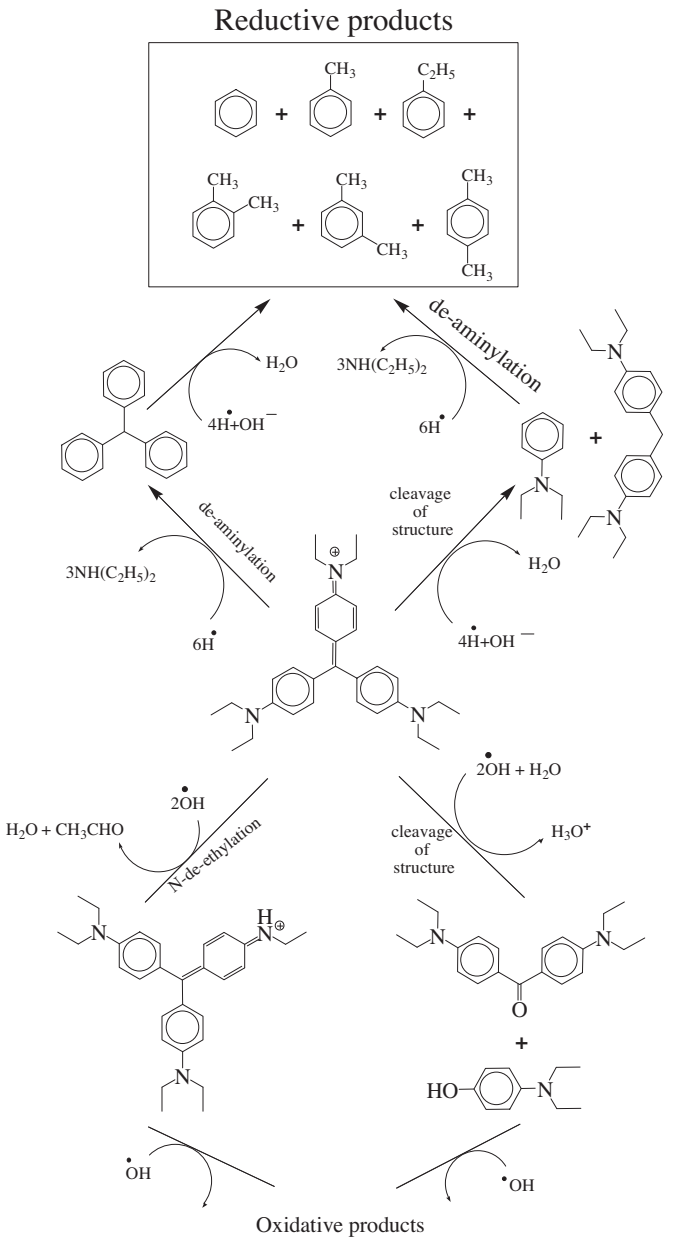

Fig. 8. Mechanisms of photocatalytic degradation under anaerobic conditions.

from the TiO_2 particle surface to the adsorbed dye through the positively charged diethylamine function and subsequence hydrolysis (or deprotonation), a nitrogen-centered radical, which was subsequently attacked by molecular oxygen to lead ultimately to de-ethylation, was yielded. The mono-de-ethylated dye, DDEPR, could also be adsorbed on the TiO_2 particle surface and implicated in other similar events (electron injection, hydrolysis or deprotonation, and oxygen attack) to yield a bi-de-ethylated dye derivative, DDPR and DEEPR. The *N*-de-ethylation process described above continued until the completely *N*-de-ethylated dye, PR, was formed.

The EV dye by photocatalysis has been extensively studied. Two possible mechanisms were suggested by previous studies (Fig. 7A) [36]. The first was a true photocatalysis process where the semiconductor was excited by light irradiation with the energy greater than its band gap energy, which caused the formation of the hole–electron pair in the semiconductor. Thus, redox reactions could provide the formation of hydroxyl radicals and superoxide ions, which were non-selective strong oxidizing agents reacting directly with the dye molecule to cause its degradation and subsequent mineralization under the aerobic condition. The EV molecule might also interact with the photogenerated holes in the valence band of the semiconductor (VB). This phenomenon provided a direct chemical reaction between the photocatalyst and the dye.

Under anaerobic conditions, a possible mechanism (Fig. 7B) was used in a photocatalytic reduction process. The conduction band delocalized the electrons through a series of reduction reactions. In this case, H_2O or H^+ absorbed the electron of conduction band so that it reached an unstable state ($H^\bullet$ atom) and $H^\bullet$ atom interacts with EV dye and then the whole conjugated chromophore structure was cloven by photocatalytic reduction when it returned to its stable energy state. During the photocatalytic process under anaerobic conditions, three competition pathways could occur simultaneously. The schemes of the mechanisms are shown in Fig. 8 with the possible reactions.

3.5.1. Photocatalytic reduction and reforming

In the photocatalytic oxidation reaction, hydroxyl radicals ($^\bullet OH$), holes (h^+), and superoxide anion radicals ($O_2^{\bullet -}$) were commonly suggested as the primary oxidizing species under aerobic conditions [36,51,52]. However, in anaerobic photocatalytic reaction conditions, $^\bullet OH$s were also formed on the TiO_2 surface, by the reaction of h^+ with OH^-; however, $O_2^{\bullet -}$ would not be generated from the reduction of O_2 by the photogenerated electrons (e^-) simultaneously. Hydroxyl radicals ($^\bullet OH$) and holes (h^+) became the main oxidants to attack the EV dye substrate. $H^\bullet$ atoms played the major reducing species to cleave the EV

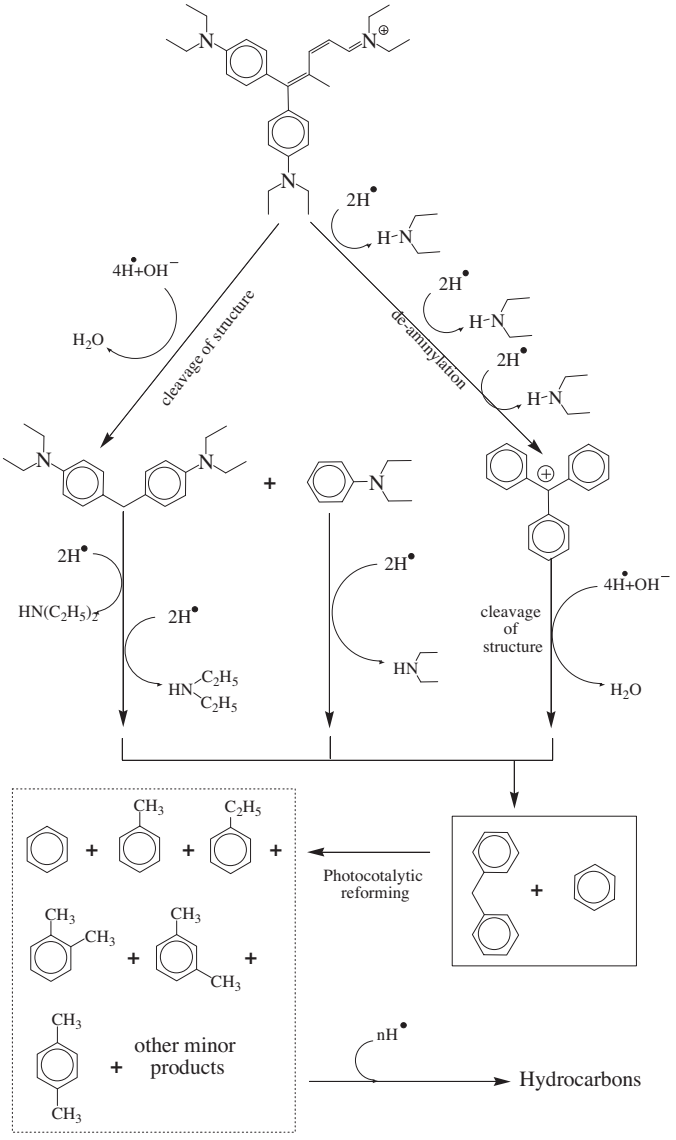

Fig. 9. Proposed mechanisms of photocatalytic reduction and reforming of the EV dye under UV irradiation and anaerobic conditions in aqueous TiO_2 dispersions followed by the identification of several intermediates by GC–MS.

dye structure and its decomposed intermediates to produce BTEX. The photocatalytic reduction and reforming mechanism of EV are proposed in Fig. 9. De-aminylation of the EV dye occurred mostly through the attack by •H atom on the *N,N′*-ethylamino portion of EV. In accord with this notion, the results showed that the triphenylmethane intermediates formed before the BTEX products did. The destruction of dye chromophore structures of the EV dye occurred mostly through the attack by •H species on the central carbon portion of EV and produced 4-(*N,N*-diethylamino)-4′-(*N′,N′*-diethylamino)methane and *N,N*-diethylaminobenzene under anaerobic conditions. Then, de-aminylation of the 4-(*N,N*-diethylamino)-4′-(*N′,N′*-diethylamino)methane and *N,N*-diethylaminobenzene occurred mostly through the attack by •H atom on the *N,N′*-ethylamino portion. Benzene and diphenylmethane would produce BTEX by photocatalytic reforming [20,22,27].

In Fig. 10, the dye molecule in the EV/TiO_2 system was adsorbed through a conjugated structure cleavage of the EV chromophore structure. Following •OH radical attack, the conjugated structure yielded a carbon-centered radical, which was subsequently attacked by molecular oxygen to lead ultimately to DDBP and DAP. The same process happened in the *N*-de-ethylated dye to produce the *N*-de-ethylated DDBP and DAP. The DDBP could also be adsorbed on the TiO_2 particle surface and be implicated in other similar events (•OH radical attraction and attack, hydrolysis or deprotonation, and/or oxygen attack) to yield a mono-*N*-de-ethylated derivative, DEBP. Moreover, the same process happened in DAP to produce EAP. The *N*-de-ethylation process as described above continued until the formation of the completely *N*-de-ethylated DDBP, BP, and *N*-de-ethylated DAP, AP. All above *N*-de-ethylation processes produced a series of *N*-de-hydroxyethylated intermediates by the hydroxylation on the *N*-ethyl group. All the intermediates were further degraded to produce *N,N*-diethylaminobenzene, *N*-ethylaminobenzene, amino-benzene, acetamide, 2-propenoic acid, and acetic acid, which were subsequently mineralized to lead to CO_3^{2-} and NO_3^- [36,53]. On the basis of all above experimental results, the pathway of photodegradation was tentatively proposed. PCR, PR, and PCO of EV took place in the presence of TiO_2 particles.

3.5.2. Oxidative degradation of EV

According to earlier reports [36,51–54], most *N*-de-alkylation processes were preceded by the formation of a nitrogen-centered radical, while the destruction of dye chromophore structures was preceded by the generation of a carbon-centered radical. Consistent with this, the degradation of EV had to occur *via* two different photodegradation pathways (destruction of the chromophore structure and *N*-de-ethylation) due to the formation of different radicals (either a carbon-centered or nitrogen-centered radical). It was no doubt that the •OH attack on the dye yielded a dye cationic radical. After this step, the cationic radical $Dye^{\bullet+}$ could undergo hydrolysis and/or follow various deprotonation pathways, which in turn were determined by different adsorption modes of EV on the TiO_2 particles surface.

On the basis of the above experimental results, the pathway of photodegradation was tentatively proposed, Fig. 10, in which the dye molecule in the EV/TiO_2 system was adsorbed through the positively charged diethylamine function. Following one •OH radical attracting a hydrogen atom from ethyl group of diethylamine and another •OH radical attacking the diethylamine radical and forming hydroxyethylated intermediates, the subsequent hydrolysis (or deprotonation) of intermediates yielded de-hydroxyethylated intermediates, which were subsequently attacked by •OH radicals to lead ultimately to *N*-de-ethylation. The mono-de-ethylated dye derivative, DDMPR, could also be adsorbed on the TiO_2 particle surface and implicated in other similar events (•OH radicals attraction and attack, hydrolysis or deprotonation) to yield a bi-de-ethylated dye derivatives, DDPR and DMMPR. The *N*-de-ethylation process as described above continued until the formation of the completely de-ethylated dye, PR.

The results not only provide evidences for the study of photocatalytic reduction with TiO_2, but also enhance our further understanding on the mechanism of photocatalytic degradation under anaerobic conditions. Based on these data, the degraded mechanism of EV is discussed and proposed. Both photocatalytic reduction and oxidation take place in the presence of TiO_2 particles. A novel photodegradation mechanism should be proposed *via* three competition pathways, including (i) cleavage of the whole conjugated chromophore structure by photocatalytic reduction, (ii) cleavage of the whole conjugated chromophore structure by photocatalytic oxidation, and (iii) *N*-de-alkylation of the chromophore skeleton.

Acknowledgment

This research was supported by the National Science Council of the Republic of China (NSC 101-2113-M-142-001-MY3).

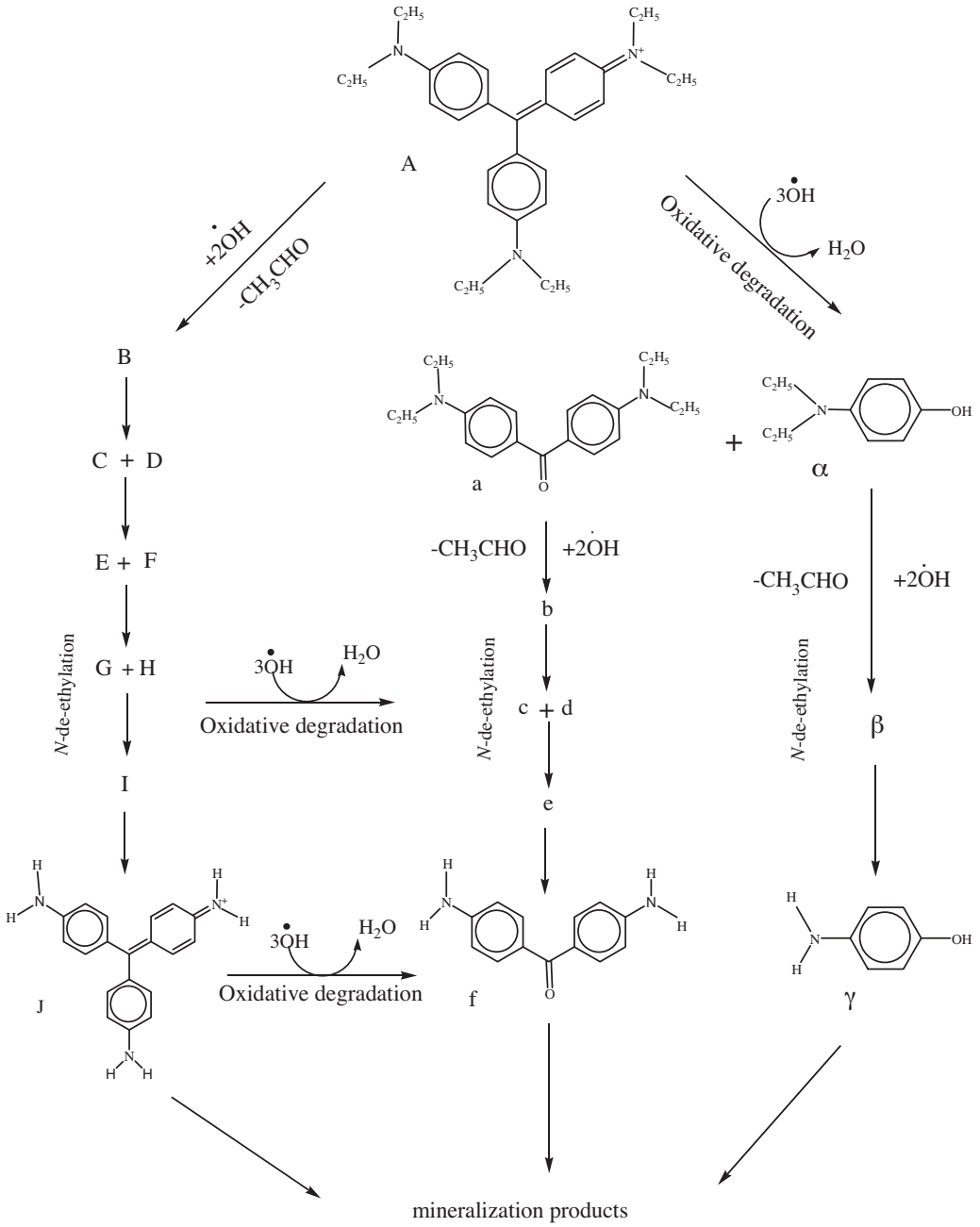

Fig. 10. Proposed photodegradation pathways of the EV dye under UV irradiation and anaerobic conditions in aqueous TiO_2 dispersions followed by the identification of several intermediates by HPLC–ESI-MS.

References

[1] Hoffmann MR, Martin ST, Choi WY, Bahnemann DW. Environmental application of semiconductor photocatalysis. Chem Rev 1995;95:69–96.

[2] Fujishima A, Rao TN, Tryk DA. Titanium dioxide photocatalysis. J Photochem Photobiol C 2000;1:1–14.

[3] Akhavan O, Ghaderia E, Rahimi K. Adverse effects of graphene incorporated in TiO_2 photocatalyst on minuscule animals under solar light irradiation. J Mater Chem 2012;22:23260–66.

[4] Zhang Y, Tang ZR, Fu X, Xu YJ. Engineering the unique 2D mat of graphene to achieve graphene–TiO_2 nanocomposite for photocatalytic selective transformation: what advantage does graphene have over its forebear carbon nanotube? ACS Nano 2011;5:7426–35.

[5] Zhang Y, Zhang N, Tang ZR, Xu YJ. Graphene transforms wide band gap ZnS to a visible light photocatalyst the new role of graphene as a macromolecular photosensitizer. ACS Nano 2012;6:9777–89.

[6] Akhavan O, Ghaderi E. Photocatalytic reduction of graphene oxide nanosheets on TiO_2 thin film for photoinactivation of bacteria in solar light irradiation. J Phys Chem C 2009;113:20214–20.

[7] Zhang N, Zhang Y, Xu YJ. Recent progress on graphene-based photocatalysts: current status and future perspectives. Nanoscale 2012;4:5792–813.

[8] Yang MQ, Xu YJ. Selective photoredox using graphene-based composite photocatalysts. Phys Chem Chem Phys 2013;15:19102–18.

[9] Zhang Y, Tang ZR, Fu X, Xu YJ. TiO_2–graphene nanocomposites for gas-phase photocatalytic degradation of volatile aromatic pollutant: is TiO_2–graphene truly different from other TiO_2–carbon composite materials? ACS Nano 2010;4:7303–14.

[10] Qi L, Yu J, Jaroniec M. Enhanced and suppressed effects of ionic liquid on the photocatalytic activity of TiO_2. Adsorption 2013;19:557–61.

[11] Lin WC, Yang WD, Jheng SY. Photocatalytic degradation of dyes in water using porous nanocrystalline titanium dioxide. J Taiwan Inst Chem Eng 2012;43:269–74.

[12] Chen CC, Lu CS, Chung YC. Photocatalytic degradation of ethyl violet in aqueous solution mediated by TiO_2 suspensions. J Photochem Photobiol A: Chem 2006;181:120–5.

[13] Dimitrijevic NM, Vijayan BK, Poluektov OG, Rajh T, Gray KA, He H, et al. Role of water and carbonates in photocatalytic transformation of CO_2 to CH_4 on titania. J Am Chem Soc 2011;133:3964–71.

[14] Hamdy MS, Amrollahi R, Sinev I, Mei B, Mul G. Strategies to design efficient silica-supported photocatalysts for reduction of CO_2. J Am Chem Soc 2014;136:594–7.
[15] Yu J, Qi L, Jaroniec M. Hydrogen production by photocatalytic water splitting over Pt/TiO_2 nanosheets with exposed (0 0 1) facets. J Phys Chem C 2010;114:13118–25.
[16] Tanaka A, Sakaguchi S, Hashimoto K, Kominami H. Preparation of Au/TiO_2 with metal cocatalysts exhibiting strong surface plasmon resonance effective for photoinduced hydrogen formation under irradiation of visible light. ACS Catal 2013;3:79–85.
[17] Maeda K. Z-scheme water splitting using two different semiconductor photocatalysts. ACS Catal 2013;3:1486–503.
[18] Kumar SG, Devi LG. Review on modified TiO_2 photocatalysis under UV/visible light: selected results and related mechanisms on interfacial charge carrier transfer dynamics. J Phys Chem A 2011;115:13211–41.
[19] Bowker M, James D, Stone P, Bennett R, Perkins N, Millard L, et al. Catalysis at the metal–support interface: exemplified by the photocatalytic reforming of methanol on Pd/TiO_2. J Catal 2003;217:427–33.
[20] Fu X, Wang X, Leung DYC, Gu Q, Chen S, Huang H. Photocatalytic reforming of biomass: a systematic study of hydrogen evolution from glucose solution. Appl Catal B: Environ 2011;106:681–8.
[21] Tanaka A, Sakaguchi S, Hashimoto K, Kominami H. Preparation of Au/TiO_2 exhibiting strong surface plasmon resonance effective for photoinduced hydrogen formation from organic and inorganic compounds under irradiation of visible light. Catal Sci Technol 2012;2:907–9.
[22] Bahruji H, Bowker M, Davies PR, Pedrono F. New insights into the mechanism of photocatalytic reforming on Pd/TiO_2. Appl Catal B: Environ 2011;107:205–9.
[23] Silva CG, Juarez R, Marino T, Molinari R, Garcia H. Influence of excitation wavelength (UV or visible light) on the photocatalytic activity of titania containing gold nanoparticles for the generation of hydrogen or oxygen from water. J Am Chem Soc 2011;133:595–602.
[24] Yuzawa H, Yoshida T, Yoshida H. Gold nanoparticles on titanium oxide effective for photocatalytic hydrogen formation under visible light. Appl Catal B 2012;115–116:294–302.
[25] Ke X, Sarina S, Zhao J, Zhang X, Chang J, Zhu H. Tuning the reduction power of supported gold nanoparticle photocatalysts for selective reductions by manipulating the wavelength of visible light irradiation. Chem Commun 2012;48:3509–11.
[26] Chiarello GL, Ferri D, Selli E. Effect of the CH_3OH/H_2O ratio on the mechanism of the gas-phase photocatalytic reforming of methanol on noble metal-modified TiO_2. J Catal 2011;280:168–77.
[27] Gua Q, Fu X, Wang X, Chen S, Leung DYC, Xie X. Photocatalytic reforming of C3-polyols for H_2 production: Part II. FTIR study on the adsorption and photocatalytic reforming reaction of 2-propanol on Pt/TiO_2. Appl Catal B: Environ 2011;106:689–96.
[28] Fu X, Long J, Wang X, Leung DYC, Ding Z, Wu L, et al. Photocatalytic reforming of biomass: a systematic study of hydrogen evolution from glucose solution. Int J Hydrogen Energy 2008;33:6484–91.
[29] Chen X, Zhou Y, Liu Q, Li Z, Liu J, Zou Z. Ultrathin, single-crystal WO_3 nanosheets by two-dimensional oriented attachment toward enhanced photocatalytic reduction of CO_2 into hydrocarbon fuels under visible light. ACS Appl Mater Interfaces 2012;4:3372–7.
[30] Roy SC, Varghese OK, Paulose M, Grimes CA. Toward solar fuels: photocatalytic conversion of carbon dioxide to hydrocarbon. ACS Nano 2010;3:1259–78.
[31] Roy SC, Varghese OK, Paulose M, Grimes CA. Toward solar fuels: photocatalytic conversion of carbon dioxide to hydrocarbons. ACS Nano 2010;4:1259–78.
[32] Liu Q, Zhou Y, Kou J, Chen X, Tian Z, Gao J, et al. High-yield synthesis of ultralong and ultrathin Zn_2GeO_4 nanoribbons toward improved photocatalytic reduction of CO_2 into renewable hydrocarbon fuel. J Am Chem Soc 2010;132:14385–87.
[33] Inoue T, Fujishima S, Konishi S, Honda K. Photoelectrocatalytic reduction of carbon dioxide in aqueous suspensions of semiconductor powders. Nature 1979;277:637–8.
[34] Mozia S, Heciak A, Morawski AW. The influence of physic-chemical properties of TiO_2 on photocatalytic generation of C_1–C_3 hydrocarbons and hydrogen from aqueous solution of acetic acid. Appl Catal B: Environ 2011;104:21–9.
[35] Yuan Q, Wu Z, Jin Y, Xu L, Xiong F, Ma Y, et al. Photocatalytic cross-coupling of methanol and formaldehyde on a rutile TiO_2 (1 1 0) surface. J Am Chem Soc 2013;135:5212–9.
[36] Chen CC, Lu CS. Photocatalytic degradation of basic violet 4: degradation efficiency, product distribution, and mechanisms. J Phys Chem C 2007;111:13922–32.
[37] Dong X, Ding W, Zhang X, Liang X. Mechanism and kinetics model of degradation of synthetic dyes by UV–vis/H_2O_2/ferrioxalate complexes. Dyes Pigments 2007;74:470–6.
[38] Lee WW, Chung WH, Huang WS, Lin WC, Lin WY, Jiang YR, et al. Photocatalytic activity and mechanism of nano-cubic barium titanate prepared by a hydrothermal method. J Taiwan Inst Chem Eng 2013;44:660–9.
[39] Chen CC, Fan HJ, Jang CY, Jan JL, Lin HD, Lu CS. Photooxidative *N*-de-methylation of crystal violet dye in aqueous nano-TiO_2 dispersions under visible light irradiation. J Photochem Photobiol A: Chem 2006;184:147–54.
[40] Chen CC, Fan HJ, Chung WH, Jan JL, Lin WY. Degradation pathways and efficiencies of acid blue 1 by photocatalytic reaction with ZnO nanopowder. J Phys Chem C 2008;112:11962–72.
[41] Xiang Q, Yu J, Wong PK. Quantitative characterization of hydroxyl radicals produced by various photocatalysts. J Colloid Interface Sci 2011;357:163–7.
[42] Ishibashi K, Fujishima A, Watanabe T, Hashimoto K. Detection of active oxidative species in TiO_2 photocatalysis using the fluorescence technique. Electrochem Commun 2000;2:207–10.
[43] Hurum DC, Agrios AG, Gray KA, Rajh T, Thurnauer MC. Explaining the enhanced photocatalytic activity of degussa P25 mixed-phase TiO_2 using EPR. J Phys Chem B 2003;107:4545–9.
[44] Wu T, Lin T, Zhao J, Hidaka H, Serpone N. TiO_2-assisted photodegradation of dyes 9. Photooxidation of a squarylium cyanine dye in aqueous dispersions under visible light irradiation. Environ Sci Technol 1999;33:1379–87.
[45] Wu T, Liu G, Zhao J, Hidaka H, Serpone N. Photoassisted degradation of dye pollutants. V. Self-photosensitized oxidative transformation of rhodamine B under visible light irradiation in aqueous TiO_2 dispersions. J Phys Chem B 1998;102:5845–51.
[46] Fan HJ, Lu CS, Jan JL, Chiou MR, Chen CC. Comparing differences of degradation pathways between P25-TiO_2 and Pt-TiO_2 mediated photocatalysis under UV irradiation. J Hazard Mater 2011;185:227–35.
[47] Liao YH, Wang JX, Lin JS, Chung WH, Lin WY, Chen CC. Synthesis photocatalytic activities and degradation mechanism of Bi_2WO_6 toward crystal violet dye. Catal Today 2011;174:148–59.
[48] Lee WW, Lin J, Chang J, Chen J, Cheng M, Chen CC. Photodegradation of CV over nanocrystalline bismuth tungstate prepared by hydrothermal synthesis. J Mol Catal A: Chem 2012;361–362:80–90.
[49] Chen KT, Lu CS, Chang TH, Lai YY, Chang TH, Wu CW, et al. Comparison of photodegradative efficiencies and mechanisms of basic blue 11 assisted by Nafion-coated and fluorinated TiO_2 photocatalysts. J Hazard Mater 2010;174:598–609.
[50] Liu G, Li X, Zhao J, Hidaka H, Serpone N. Photooxidation pathway of sulforhodamine-B. Dependence on the adsorption mode on TiO_2 exposed to visible light radiation. Environ Sci Technol 2000;34:3982–90.
[51] Mai FD, Lee WWL, Chang JL, Liu SC, Wu CW, Chen CC. Fabrication of porous TiO_2 film on Ti foil by hydrothermal process, and its photocatalytic efficiency and mechanisms with Ethyl Violet Dye. J Hazard Mater 2010;177:864–75.
[52] Chen CC. Degradation pathways of ethyl violet by photocatalytic reaction with ZnO dispersions. J Mol Catal A: Chem 2007;264:82–92.
[53] Fan H, Lu C, Jan J, Chiou M, Chen CC. Comparing differences of degradation pathways between P25-TiO_2 and Pt-TiO_2 mediated photocatalysis under UV irradiation. J Hazard Mater 2011;185:227–35.
[54] Liao YH, Wang JX, Lin JS, Chung WH, Lin WY, Chen CC. Synthesis, photocatalytic activities and degradation mechanism of Bi_2WO_6 toward crystal violet dye. Catal Today 2011;174:148–59.